

Highly adherent bioactive glass thin films synthesized by magnetron sputtering at low temperature

G. E. Stan · I. Pasuk · M. A. Husanu · I. Enculescu ·
S. Pina · A. F. Lemos · D. U. Tulyaganov ·
K. El Mabrouk · J. M. F. Ferreira

Received: 22 June 2011 / Accepted: 29 August 2011 / Published online: 14 September 2011
© Springer Science+Business Media, LLC 2011

Abstract Thin (380–510 nm) films of a low silica content bioglass with MgO, B₂O₃, and CaF₂ as additives were deposited at low-temperature (150°C) by radio-frequency magnetron sputtering onto titanium substrates. The influence of sputtering conditions on morphology, structure, composition, bonding strength and in vitro bioactivity of sputtered bioglass films was investigated. Excellent pull-out adherence (~73 MPa) was obtained when using a 0.3 Pa argon sputtering pressure (BG-a). The adherence declined (~46 MPa) upon increasing the working pressure to 0.4 Pa (BG-b) or when using a reactive gas mixture (~50 MPa). The SBF tests clearly demonstrated strong biomineralization features for all bioglass sputtered films. The biomineralization rate increased from BG-a to BG-b, and yet more for BG-c. A well-crystallized calcium hydrogen phosphate-like phase was observed after 3 and 15 days of immersion in SBF in all bioglass layers, which transformed monotonously into hydroxyapatite under prolonged SBF immersion. Alkali and alkali-earth salts (NaCl,

KCl and CaCO₃) were also found at the surface of samples soaked in SBF for 30 days. The study indicated that features such as composition, structure, adherence and bioactivity of bioglass films can be tailored simply by altering the magnetron sputtering working conditions, proving that this less explored technique is a promising alternative for preparing implant-type coatings.

1 Introduction

Since their discovery, bioglasses have proved their suitability to form a bond with the living bone tissue by enhancing the osteosynthesis at the implant site due to favourable chemical interactions with the body fluid in the tissue rehabilitation process [1]. Therefore, considerable attention has been given to the use of implants with bioactive fixation in the past decade [2]. Bioactive glasses and glass-ceramics have been extensively developed and investigated for applications as bone grafts or fillers owing to their ability to form a bond to living bone and put into clinical use following many years of animal testing in a variety of experimental models [3–5]. The dissolution of the glass network, leading to the formation of a silica-rich gel layer and subsequent deposition of an apatite-like layer on the glass surface, were found to be essential steps in the bioactivity evaluation by both in vivo and in vitro studies [6, 7]. The formation of stable, mechanically strong interface with both bone and soft connective tissues is essential for the clinical success [8–11].

In this work we aimed to study the bioactivity of bioglass as coatings prepared by magnetron sputtering technique. Only very few results have reported on bioactive bioglass thin films deposited onto titanium substrates. The existing reports are rather short and inconclusive [12–17]. Generally,

G. E. Stan (✉) · I. Pasuk · M. A. Husanu · I. Enculescu
National Institute of Materials Physics, P.O. Box MG-7,
077125 Bucharest-Magurele, Romania
e-mail: george_stan@infim.ro

S. Pina · A. F. Lemos · D. U. Tulyaganov · J. M. F. Ferreira
Department of Ceramics and Glass Engineering,
CICECO, University of Aveiro, Aveiro, Portugal

D. U. Tulyaganov
Turin Polytechnic University in Tashkent, Tashkent, Uzbekistan
700174

K. El Mabrouk
Institute of Nanomaterials and Nanotechnology, ENSET,
Av. de l'Armée Royale, Madinat El Irfane, 10 100 Rabat,
Morocco

low values of adhesion for such structures were published [16, 17]. An impediment in using bioglass coatings as implant applications is the high thermal expansion coefficients of bioglass, about $14\text{--}15 \times 10^{-6}/^\circ\text{C}$, relative to that of medical-grade titanium $\sim 9.2 \times 10^{-6}/^\circ\text{C}$ [17]. Among the deposition techniques available for producing bioglass coatings, magnetron sputtering is the less explored. Only three articles have been published on this topic at the best of our knowledge [16, 18, 19].

Radio frequency-magnetron sputtering (RF-MS) is a flexible technique that allows the efficient sputtering of almost any compound, high bonding strength of films, good quality coverage of steps or small features and automation. Uniform and high-purity adherent films on large areas can be easily deposited by this technique [20]. The present study shows that magnetron sputtering is a reliable deposition technique for obtaining highly adherent and bioactive bioglass coatings onto titanium substrates at low temperatures, without subsequent thermal treatment after deposition, avoiding the mechanical failure caused by the thermal conductivity mismatch. A novel fine glass powder with composition based on $\text{SiO}_2\text{--CaO--MgO--P}_2\text{O}_5\text{--CaF}_2\text{--B}_2\text{O}_3\text{--Na}_2\text{O}$ system was used as deposition cathode target [21].

The main goal was studying the effects of sputtering pressure, composition of working atmosphere and deposition parameters on the compositional, morpho-structural and mechanical properties of the coated implants, and their influence on the *in vitro* behaviour of the coatings in simulated body fluid (SBF). Understanding these correlations is important for biomaterials science, implantology, as well as from applied physics and technological point of view.

2 Materials and methods

2.1 Deposition procedure

A new recently developed of bioactive glass composition [21] was used, which is based on the $\text{SiO}_2\text{--CaO--MgO}$ system, with P_2O_5 , CaF_2 , B_2O_3 , and Na_2O as additives having the following overall composition (wt%): $\text{SiO}_2\text{--}40.08$, $\text{CaO--}29.1$, $\text{MgO--}8.96$, $\text{P}_2\text{O}_5\text{--}6.32$, $\text{CaF}_2\text{--}5.79$, $\text{B}_2\text{O}_3\text{--}5.16$, and $\text{Na}_2\text{O--}4.59$.

Bioglass targets (110 mm diameter, 3 mm thick) were manufactured by cold pressing from as-prepared powders [21, 22]. Mirror polished square pieces of Ti grade 1 (Mateck GmbH) having an area of $10 \times 10 \text{ mm}^2$ were used as substrates. In order to estimate the films' thickness by a method based on optical transmittance measurement [23], parallel depositions were done also on Corning glass substrates. The substrates were ultrasonically cleaned successively in acetone and ethanol for 10 min in an ultrasonic bath before being mechanically fixed into the deposition chamber in an aluminium holder at a 35 mm target-to-substrate distance.

BG films were sputtered using a UVN-75R1 (1.78 MHz) deposition system having a magnetron cathode with a plasma ring of ~ 55 mm diameter. The sputtering chamber was first evacuated to a pressure less than 2×10^{-3} Pa. Then spectral argon and oxygen were admitted through needle valves at various flow rates in order to obtain the desired deposition atmospheres at various oxygen dilutions and total pressures. A constant total gas flow rate of 45 standard cubic centimetres per minute (sccm) was used for all depositions. Prior to deposition the substrates were plasma etched in argon atmosphere for 10 min in order to improve films adhesion [24]. During the magnetron sputtering process the pressure was measured by a capacitive gauge (Alcatel ASD 1004) and the temperature ($\sim 150^\circ\text{C}$) was estimated with a Chromel-Alumel thermocouple. Two different working pressures and/or atmospheres were used (Table 1). The sputtering of BG coatings onto titanium and glass substrates was carried out for 70 min in all experiments.

2.2 Structural, morphological and compositional characterization

Information on bonding configuration in the bioglass powder and in the as-deposited coatings was obtained by Fourier transform infrared (FTIR) spectroscopy (model Mattson Galaxy S-7000, USA) in diffusion reflectance mode. The analysis was performed within the range $400\text{--}4000 \text{ cm}^{-1}$, with a 4 cm^{-1} resolution, with a total of 32 scans per experiment. Prior to the calculation of specific FTIR vibrational bands' areas, a background subtraction was performed. The FTIR peak parameters (peak position and area) were determined using a mixed Gaussian-Lorentzian function in the Origin Pro 8 peak-fitting procedure.

Table 1 Deposition conditions and thicknesses of bioglass films

Sample batch	Total pressure (Pa)	Working atmosphere	Gas flow (sccm)	Deposition time (min)	Thickness (nm)
BG-a	0.3	100% Ar	45	70	510
BG-b	0.4	100% Ar	45	70	480
BG-c	0.3	93%Ar + 7%O ₂	45	70	380

The identification of the crystalline phases in the soaked samples was done by X-ray diffraction using a Bruker D8 Advance diffractometer, in powder setting, with Cu K α ($\lambda = 1.5418 \text{ \AA}$) radiation. The diffractometer was equipped with a high efficiency one-dimensional detector (Lynx Eye type) operated in integration mode. Samples were spin at 15 rpm during overnight data collection in order to average over possible inhomogeneities of the surface layer and because of the very low intensity scattered radiation.

The surface morphology of the films was examined using scanning electron microscopy (FE-SEM Hitachi S-4100, Japan; 25 kV acceleration voltage, beam current 10 μA) under secondary electron mode. The tilt-SEM images were recorded at 30° in order to estimate the thickness of the chemically grown hydroxyapatite (HA) layers.

The layer thicknesses were estimated from optical spectroscopy transmittance according to the Swanepoel procedure [23]. This method is based on optical transmittance measurements in the non-absorbance and low absorption region, for films deposited onto glass substrates. The transmittance measurements were performed using a Perkin-Elmer UV-VIS-NIR Lambda 90 spectrophotometer in the wavelength range from 300 to 800 nm.

Chemical composition analyses were carried out by X-ray photoelectron spectroscopy (XPS) in a complex Specs GmbH surface science setup, including a photoemission chamber. XPS is a powerful tool whose sensitivity allows emphasizing the differences in chemical environment among oxygen atoms in oxide glasses, offering quantitative information in relation with the local structural order or bonding configuration. The base pressure in the whole system was in the 10^{-8} Pa range. The BG samples were analyzed by using unmonochromatized Al K α radiation (1486.6 eV). The XPS survey spectra were recorded as well as high resolution core level scans for the C 1s, Si 2p and O 1s photoelectron peaks. The analysis was performed on three different regions of the samples' surface (randomly selected), and the results were very similar. The Phoibos 150 mm radius electron analyzer was operated at 90 eV pass energy for survey spectra, and at 20 eV pass energy for the high-resolution individual core level scans. During the measurement, an electron flood gun operating at 3 eV acceleration energy and 0.3 mA emission current was used, in order to ensure the neutralization of the surface charge (charge compensation) and to prevent an eventual drift of the XPS lines. This was systematically checked on C 1s spectra on reference samples and the observed energy shifts are lower than 0.1 eV. The area imaged by the photoelectron detector is of $\sim 14 \text{ mm}^2$. The position and peak fitting of photoelectron maximum were estimated using spectra simulation based on the convolution of Lorentzian and Gaussian functions [25, 26].

One cannot consider the effective sampling depth ($\sim 2 \text{ nm}$) of the XPS technique as reliable for determining with accuracy the bulk composition of the whole BG coatings. This was the reason why more reliable compositional data were extracted from EDS technique. The near surface region analyzed in XPS should have a structural and chemical integrity closely approaching that of the bulk film, which is highly improbable when dealing with disordered materials such as glasses. Thus, for estimating the average composition of the BG films, energy-dispersive X-ray spectroscopy (EDS) measurements were performed with a Bruker-AXS 133 eV XFlash[®] 4010 instrument on the as-sputtered and soaked samples. In order to check for the experimental reproducibility, EDS analysis were performed in duplicate, making measurements on five different regions of $20 \times 20 \mu\text{m}$. The results were analyzed separately, and both sets of experiments had comparable results. For this reason only results from one of the two sample batches are presented in the article.

2.3 Pull-out bonding strength measurements

The pull-out measurements were carried out using an adhesion tester-DFD Instruments PAT MICRO adhesion tester AT101 (maximum pull force = 1 kN) equipped with $\Phi 2.8 \text{ mm}$ stainless steel test elements. The test elements were glued to the film's surface with a cyanoacrylate one-component Epoxy adhesive, E1100S. The stub surface was first polished, ultrasonically degreased in acetone and ethanol and dried in a nitrogen flow. After gluing, the samples were placed in an oven for thermal curing (130°C/1 h). Each test element was pulled-out vertically with a calibrated hydraulic pump until detachment. The experimental procedure was conducted in accordance with the ASTM D4541 and ISO 4624 standards. The adhesion strength was determined from the recorded failure value divided by the quantified detached surface area. Mean values and standard deviations were computed. The statistical significance was determined using an unpaired Student's *t* test. The differences were considered significant when $P < 0.05$.

2.4 In vitro analysis in simulated body fluid

The in vitro bioactivity of as-deposited samples, reflected in their capability of inducing HA-formation onto their surfaces, was investigated by immersion in SBF at 37°C for various periods of time. Polished Ti substrates were used as control samples. The SBF had the following ionic concentrations (in mM) of 142.0 Na⁺, 5.0 K⁺, 2.5 Ca²⁺, 1.5 Mg²⁺, 147.8 Cl⁻, 4.2 HCO₃⁻, 1.0 HPO₄²⁻ and 0.5 SO₄²⁻, buffered at pH = 7.25 with tris-hydroxymethyl-aminomethane (Tris, 50 mM) and hydrochloric acid solutions according to Kokubo [27, 28]. The SBF was filtered

through sterilized filters (cameo 25 AS-MSI, pore size 0.22 μm). A surface area to volume ratio of 0.1 cm^{-1} was maintained for all immersions, and the SBF solutions were not exchanged during the experiments. The samples were removed from the incubator, rinsed gently, first with pure ethanol and then using deionized water, and left to dry at ambient temperature in a desiccator for 3 h.

Sampling took place at 3, 15 and 30 days and the mineralization capability of inducing HA-formation onto the coated surfaces was evaluated as described below. Changes in coatings morphology, crystalline structure and composition were monitored by SEM-EDS, FTIR and XRD measurements. We studied the influence of the deposition atmosphere and pressure expecting important modifications of the BG layer structure, adhesion and bioactivity. The thickness of the chemical grown HA layers was estimated by tilt-SEM technique.

3 Results

3.1 Thickness determination

The deposition conditions of the BG films and the respective thickness values estimated by the Swanepoel procedure are displayed in Table 1. One can notice that film thickness decreases with increasing total pressure or when admitting oxygen in the working chamber.

3.2 Pull-out bonding strength results

The adhesion strength at the coating—substrate interface is a critical factor in successful implantation and long-term

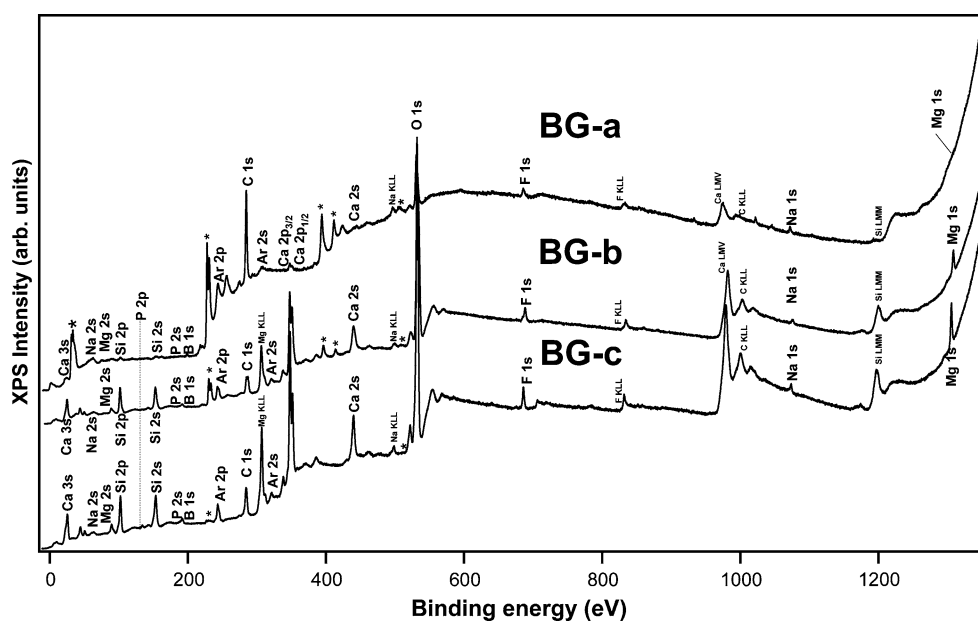
stability of such implant-type structures. Ten samples were tested for each type of structure, the data being represented as mean \pm standard deviation.

For BG-a coatings, an average bonding strength value of 72.6 ± 2.9 MPa has been recorded, the failure always occurring at the film—substrate interface. This bonding strength value is much higher than the ones usually reported in literature [16, 17, 29]. For the films deposited at higher argon pressure (BG-b), the adherence dramatically decreased to a mean value of 45.7 ± 5.0 MPa, the bonding failure occurring at the film—substrate interface. When using a reactive atmosphere, but keeping total pressure constant value of 0.3 Pa, the adhesion strength of monolithic BG coating declined to 52.3 ± 3.0 MPa (BG-c). Similar adherence values have been generally reported in literature [16, 17, 29]. The two tailed *t* testing, assuming unequal variances, showed statistically significant differences between the recorded adherence values ($P < 0.05$). The excellent adherence value of BG-a/Ti coatings offering new perspectives in implantology, must be emphasized.

3.3 XPS analysis

The survey scans performed on three randomly selected regions for each BG sample surface were similar, demonstrating the BG surface homogeneity. Only some representative spectra are presented (Figs. 1, 2). The XPS survey scans of the as-deposited bioglass films' surfaces are shown in Fig. 1, while the high resolution spectra of O 1s and Si 2p are presented in Fig. 2. The experimental peak positions found in the survey scans as well as the O 1s peak fitting results (peak fitted components positions and full width at half maximum (FWHM)) are collected Table 2.

Fig. 1 XPS survey scans of the as-deposited bioglass samples



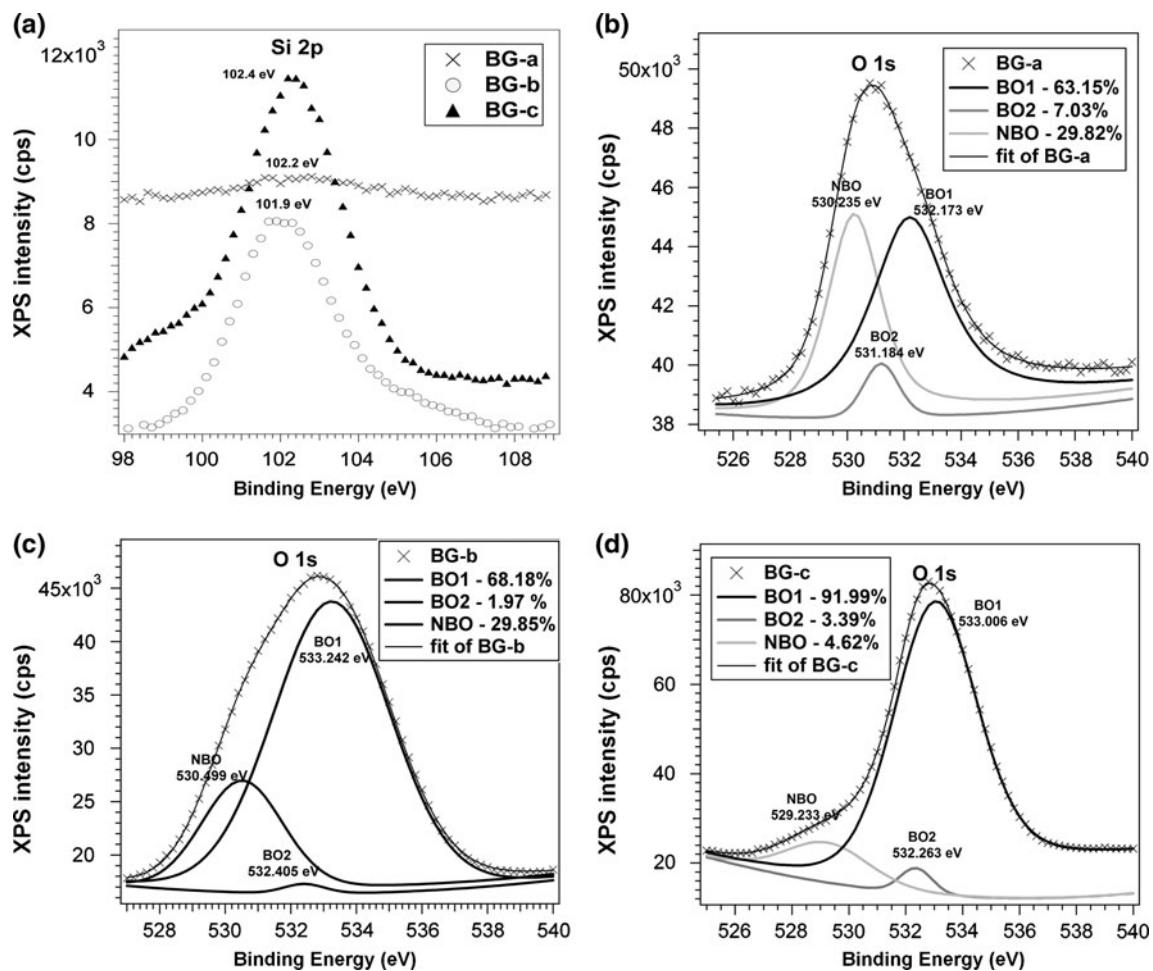


Fig. 2 High resolution XPS spectra. Si 2p core level photoelectron: **a** all BG films; O 1s core level photoelectron: **b** BG-a, **c** BG-b, **d** BG-c

The lines labelled with (*) are due to the molybdenum clamps fixing the sample on the holder. The complex bonding mechanism between different chemical species which in turn modifies the properties of the bioglasses is accompanied by changes of the elements chemical state. These changes are reflected in slight variations of spectral lines, peak position and shape (Fig. 1; Table 2). One key parameter tailoring the properties of BG's is known to be the network formers/network modifiers ratio [30].

The Si 2p photoelectron spectra for the as-deposited BG films are shown in Fig. 2a. One can notice that the Si 2p signal shifts towards lower energies (from 102.2 to 101.9 eV) when increasing the argon sputtering pressure, and to higher energies (102.4 eV) when oxygen was admitted in the working atmosphere. The lower intensity of Si 2p line in case of BG-a, denotes a curtailed Si/O atomic ratio at the surface, this sample surface being enriched in phosphorous, sodium, and fluorine (data not presented). The narrowing of Si 2p lines in case of BG-c denotes a higher ordering of the silicon neighbourhood. Usually the binding energy (BE) increases with SiO₂ content and

reflects a decreased electron charge density around silicon atoms that is expected to be shifted toward oxygen atoms.

A similar behaviour has been observed for the O 1s photoelectron peak, as shown in Fig. 2b–d. These O1s photoelectron peaks provide us with very useful information because the oxides in the silicate glasses have different

Table 2 Peak positions in the experimental XPS survey spectra of the BG as-deposited films

Element line	BG-a position (eV)	BG-b position (eV)	BG-c position (eV)
Si 2p	102.2	101.9	102.4
Ca 2p _{3/2}	347.6	345	349
P 2p	132.8	133.2	135
B 1s	191.6	188.8	192.1
Na 1s	1071.8	1071.6	1071.8
Mg 1s	1303.8	1306	1305.6
F 1s	685.6	685.8	686.8
C 1s	284.5	284.5	284.5
O 1s	531.2	531.1	531.9

types of chemical bonds. The silica-based glass generally consists of two kinds of oxygen atoms: covalently bonded bridging oxygen (BO) atoms that connect two SiO_4 tetrahedra, and non-bridging oxygen (NBO) atoms that are covalently bonded to one SiO_4 tetrahedron and ionically bonded to one alkali or alkaline earth ion. The BO and NBO oxygen atoms appear as two components in the O 1s peak, with the BO atoms having higher binding energy than the NBO atoms [30, 31]. The peak ascribed to oxygen in the non-bridging position occurs generally at lower BE by 1.7–2.8 eV than the peak due to BO atoms depending on the alkali ions present in the glass [32]. On the other hand, phosphorous and boron could act in the glass structures as network formers. In another study Bunker et al. were able to follow the effects of composition on four different oxygens in sodium borosilicate glasses: Si–O– Na^+ , Si–O–Si, B–O–Si, and B–O–B [33, 34].

The peak fitting studies of the O 1s spectra revealed three distinct peaks. One can hypothesize that the “BO peak” is complex and can be resolved into two components: a higher energy shoulder, BO1, corresponding to the Si–O–Si bonds and a lower energy shoulder, BO2, associated with P–O–Si and B–O–Si possible bonds. Similar observations have been made for different compositional glass systems [35, 36]. The measured areas of BO1, BO2 and NBO peaks are displayed on the graphs. Other peak fitting results (peak components positions and FWHM) of the O 1s XPS spectra are shown in Table 3. The samples deposited in inert atmosphere exhibit comparable amounts of BO and NBO, while bridging oxygen (BO) atoms predominate (~95% in case of BG-c) in the samples deposited under reactive atmosphere. Considering the effective sampling depth (2 nm), the absence of the inelastic tail associated with the BO1 component (Fig. 2d) suggests that the XPS signal is related with the outer SiO_2 -rich atomic layers, while the NBO and BO2 components, featured by an inelastic tail in their XPS spectrum, are associated with atomic layers located below the BO1-rich layer [25, 37]. The XPS results, which are consistent with our SEM investigations, will be discussed further.

3.4 SEM-EDS results

Figure 3 displays the SEM micrographs of the as-deposited BG films. One can see important modifications of the

morphology at a sub-micrometric level when varying the deposition conditions. The SEM micrographs revealed well-adhered films with homogeneous fine surface microstructures for all as-deposited samples. No signs of microcracks or delaminations were noticed. The working pressure seems to have little influence on the microstructure (BG-a and BG-b). The surfaces of BG-a and BG-b are generally smooth and consist of nano-sized merged granules indicative of a uniform growth. However, the BG-b samples also display some round-shaped in-growths in the films' mass having diameters between 0.1 and 1 μm . The formation of larger aggregates could be explained by a process of surface energy minimization. At higher pressure the transverse diffusivity of the atoms is reduced, due to a lower energy of ad-atoms that deposit on the growing film. In such cases any morphological obstacle becomes difficult to surpass, favouring atoms to agglomerate.

In case of reactive atmosphere (BG-c) the films' surfaces presented interesting features. The BG-c coatings were uniformly covered by tower-shaped nano-formations with an average diameter of ~70 nm. The tower-shaped nano-aggregates seem to be ingrowths nucleated on a matrix, like observed in less extension in the BG-a and BG-b films. Such nanostructured morphology could be favourable to osteoblast cells adhesion as reported before [38, 39]. It was shown that the shift from micro-to-nanometer sized topology could result in increasing osteoblast cellular activity [39, 40]. Besides the increase in surface area, nanoscale roughness of materials might allow unique energetics due to altered electron delocalizations or surface defects [38].

Figure 4 shows the morphological changes occurred at the surface of the bioglass coatings after 3, 15 and 30 days of immersion in SBF. After 3 days of immersion, the morphologies of the BG films display signs of an incipient precipitation process, along with features of leaching-dissolution phenomena that took place within this early incubation stage. The leaching is more evident in case of BG-a, which shows a pitched surface with a high density of indents, while in case of BG-b and yet more for BG-c, these indents seem to be covered by a fine precipitated layer. Thus the precipitation process seems to be in a more advanced stage for the films deposited under higher pressure (BG-b) and even more under a reactive atmosphere (BG-c). At this point one can deduce that the mineralization process is faster for the film deposited under reactive

Table 3 The O 1s core level photoelectron peak fitting results

	Sample								
	BG-a			BG-b			BG-c		
Peak component	BO1	BO2	NBO	BO1	BO2	NBO	BO1	BO2	NBO
Position (eV)	532.2	531.2	530.2	533.2	532.4	530.5	533.0	532.2	529.2
FWHM (eV)	3.8	1.6	2.5	4.1	1.2	2.8	3.4	1.4	2.4

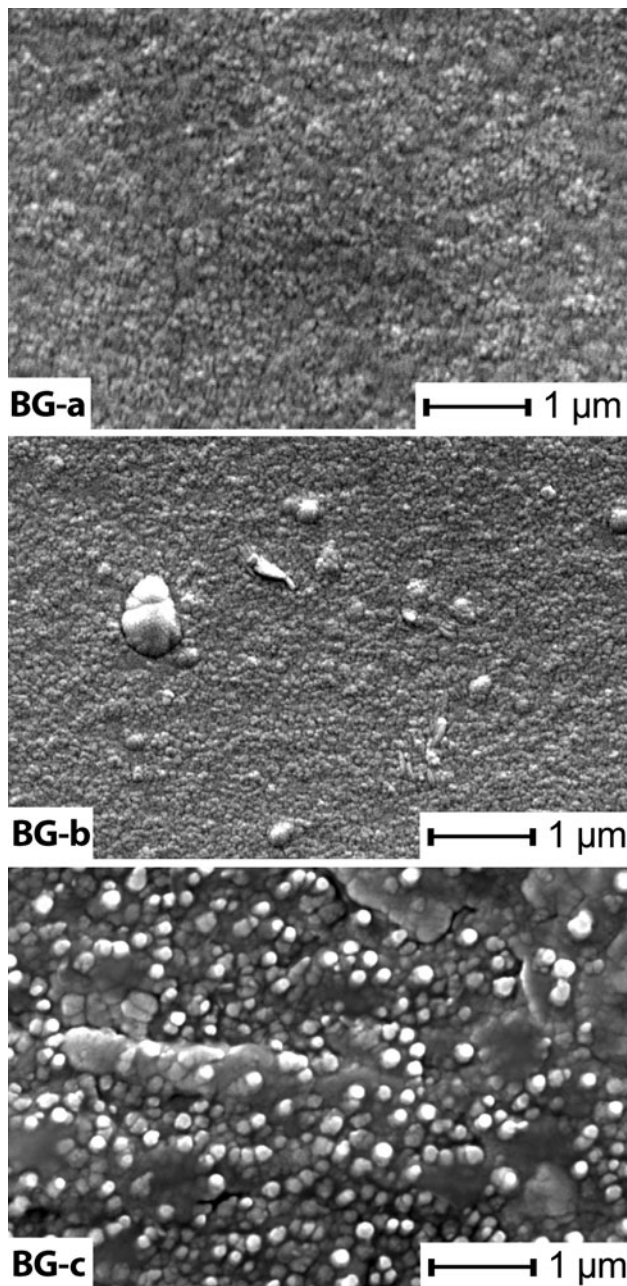


Fig. 3 SEM images of as-deposited bioglass sputtered films

atmosphere. A prolonged immersion of 15 days leads to an extensive precipitated layer covering the entire surface of the BG films, with BG samples presenting negligible surface morphology differences.

The SEM microstructures of BG films immersed for 30 days clearly asserted the growth of thick and rough coatings on top of all three types of samples, typical for SBF apatitic in-growths [4], evidencing good biomineralization capability of these BG coatings. BG-b and BG-c display a rough surface containing spherulitic grains with diameters ranging between 1.7 and 2.4 μm . BG-a displays

a different topographic aspect having a smoother surface with homogeneously distributed agglomerates of nano-sized spherulites.

The surface morphology of Ti control substrates remained unchanged along the entire immersion time period tested (30 days). However a few light coloured randomly distributed cubic crystals, revealed by EDS as NaCl, were seen on the metallic surface (Fig. 4-bottom).

The tilt-SEM thickness measurements of the chemical grown HA layers performed in several regions of each film revealed similar values for the estimated thickness. Figure 5 shows some representative images. The thickest chemical growths were observed for the BG-b and BG-c coatings, which exhibit average total film thickness values of $\sim 1.1 \mu\text{m}$ and of $\sim 1.8 \mu\text{m}$, respectively. But, it is worth mentioning that we found also film regions with extreme thickness of $\sim 0.8 \mu\text{m}$ and $\sim 2 \mu\text{m}$ for BG-b, and of $\sim 1.3 \mu\text{m}$ and $\sim 3.4 \mu\text{m}$ for BG-c, compared to the as-deposited film thickness of $\sim 0.4 \mu\text{m}$. The thickness of BG-a films increased upon immersion in SBF for 30 days from $\sim 0.5 \mu\text{m}$ to $\sim 0.75 \mu\text{m}$. Thus, the best biomineralization, correlated with the thickest HA layer growth, was obtained for the BG-c coating. The results are in agreement with the FTIR and XRD analysis presented herein.

The EDS data of the as-deposited samples are presented in Table 4. The results for the lightest elements (boron and fluorine) were not included because of their expected lower accuracy. One can notice that the target composition is not stoichiometrically transferred to the films. Such an effect might be explained by the glass network rearrangement occurring during the film growth, which is associated to physical processes of magnetron sputtering and to the complex structure of the target material. Even considering the low accuracy of EDS analysis, some conclusions could be drawn. The silicon content decreased from $\sim 38 \text{ at.}\%$ in the starting BG powder to $\sim 30 \text{ at.}\%$, for BG films. Under inert atmosphere, a quasi-stoichiometric transfer of calcium occurred, while there was a progressive depletion in phosphorous to $\sim 50\%$ at 0.3 Pa and to less than 20% at 0.4 Pa. These variations were accompanied by a clear enrichment of the as-deposited BG films in sodium (about two times, favoured by an increase of Ar pressure) and in magnesium of ~ 1.4 and ~ 1.3 times for 0.3 and 0.4 Pa, respectively, relative to the target powder. On the other hand, the presence of oxygen in the working atmosphere and the total pressure of 0.3 Pa exerted strong effects on films' composition. In the presence of the oxygen reactive atmosphere the Na content was strongly enhanced (~ 3.2 times), with Ca showing an opposite trend decreasing with $\sim 60\%$, while Mg shows a general increase of ~ 1.5 times relative to the target powder. It seems reasonable to hypothesize that the atomic mass and the affinity of the different elements towards oxygen, as well as the total

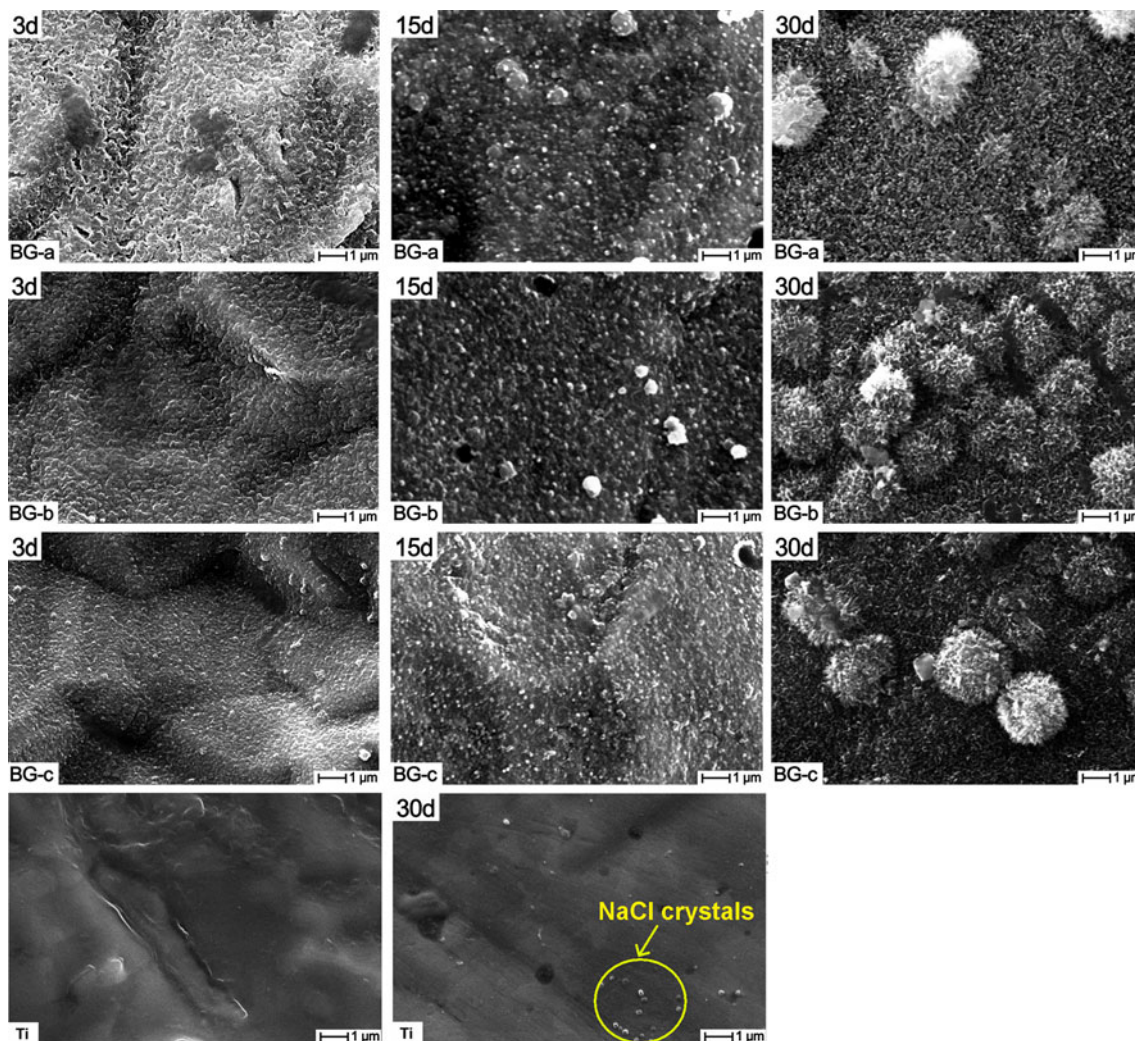


Fig. 4 SEM images of the surfaces of the bioglass sputtered films after immersion in SBF for 3, 15 and 30 days, and of the titanium control samples before and after 30 days of immersion in SBF

pressure that determines the number of atomic collisions per unit of time will affect the deposition behaviour. However, the observed compositional variations are not yet fully understood and should be regarded with care.

The results of EDS analyses of the samples immersed in SBF for different time periods are displayed in Fig. 6. It seems clear that Ca and P are the most abundant elements at the surface of soaked BG films, showing a general increase with immersion time, in good agreement with the apatite-like nature of deposited layers of increased thickness as observed in the SEM microstructures of Figs. 4 and 5.

The EDS measurements asserted the bioactive behaviour of the BG films. Considering that during the dissolution–precipitation process the BG films are only partially dissolved [14, 41], EDS results reflect the combined contribution of the seed film and of the chemically grown apatitic layer.

The decreasing trends observed for Si, Mg and Na after 3 days of soaking, contrasting with increases in Ca and P, are in good agreement with the first stages of Hench's theory: leaching of the glass ions, loss of soluble silica in the form of $\text{Si}(\text{OH})_4$ to the solution resulting from the breakdown of Si–O–Si bonds, and followed by the migration of Ca^{2+} and $(\text{PO}_4)^{3-}$ to the surface to form $\text{CaO–P}_2\text{O}_5$ film. For BG-a, EDS results suggest a tardy bioactive process. After 15 days of immersion the Ca and P films' concentration is constant, suggesting that an equilibrium ratio Ca/P has been attained. From this moment on, the precipitated $\text{CaO–P}_2\text{O}_5$ film undergoes structuring and ordering phenomena, resulting in calcium phosphates formation, and further crystallization in a carbonated hydroxyapatite layer, as shown by FTIR and XRD hereunder. After 15 days, an increase of Na concentration was observed along with the detection of chlorine (not represented). After 30 days of immersion in SBF the Ca/P ratios of apatitic layers grown

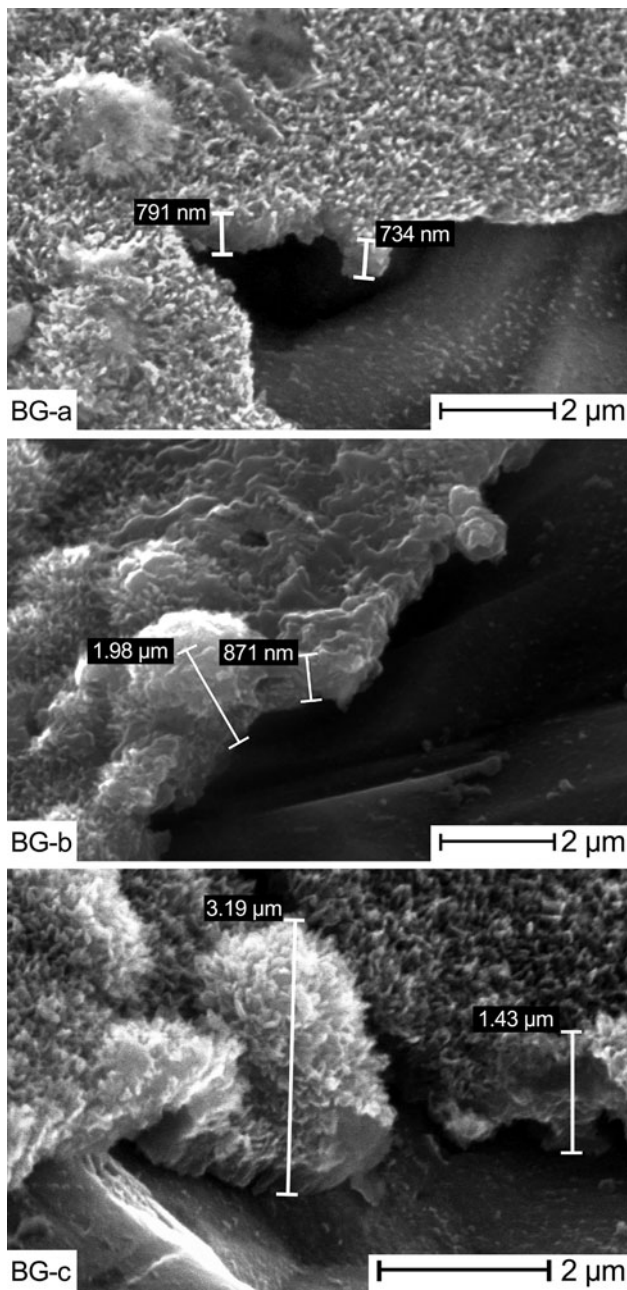


Fig. 5 SEM images of the bioglass sputtered films immersed for 30 days viewed in tilt mode

on the surface of BG films under biomimetic conditions presented similar values (~ 1.5), very close to that of stoichiometric tricalcium phosphate, suggesting that a calcium deficient apatite has been deposited.

3.5 FTIR characterizations

Fourier transform infrared spectroscopy measurements were used to analyze the nature of the as-deposited and chemical growth films in SBF in vitro environment. The

Table 4 Chemical compositions in at% for the BG target powder and for the BG films deposited onto titanium substrates

Element	Target powder	BG-a	BG-b	BG-c
Si	38.43	30.58 ± 0.84	30.27 ± 0.61	30.47 ± 0.51
Ca	34.18	31.96 ± 1.16	32.59 ± 1.14	19.89 ± 1.00
P	5.90	2.85 ± 0.67	1.12 ± 0.18	3.15 ± 0.65
Na	8.50	16.16 ± 0.71	19.40 ± 0.86	27.07 ± 1.00
Mg	12.88	18.45 ± 0.97	16.62 ± 0.83	19.42 ± 1.15

The values were determined by EDS for the films, and were calculated on the basis of the nominal oxides composition for the target. The data were represented as mean ± standard deviation ($n = 5$)

infrared absorption spectra of the as-deposited bioglass films are presented together with the spectrum of the target powder (Fig. 7). All spectra display a broad absorption band with two peak maxima at $\sim 1030\text{ cm}^{-1}$ (Si–O stretching in Q^2 and Q^3 units) and $\sim 940\text{ cm}^{-1}$ (Si–O stretching Q^1 and Q^2 units). A weak shoulder corresponding to Si–O–Si bending motion was found at $\sim 725\text{ cm}^{-1}$. Broad vibration bands centred at 1218 and 1411 cm^{-1} were evidenced, most probably due to the vibration of metaborate triangles. Previous IR studies noticed also the presence of Q^2 , Q^1 , and Q^0 phosphate units in the $400\text{--}1400\text{ cm}^{-1}$ IR spectra range [20, 42]. Line positions and their assignments for the most intense ones are displayed in Table 5.

Figure 8 displays the evolution of the FTIR spectra for the BG structures after SBF immersions for 3, 15 and 30 days. Similar IR spectral evolutions were observed for BG films, in agreement with the results of EDS and SEM observations. A change of the BG spectra envelope was noticed after 3 days of immersion in SBF (Fig. 8a). There are some perceptible differences in shape and amplitude of the IR spectra between these three investigated glass films. The two dominant maxima (~ 1090 and $\sim 1120\text{ cm}^{-1}$, respectively) could be assigned to the juxtaposition of the $(\text{PO}_4)^{3-}$ (ν_3) asymmetric stretching bands and the acid phosphate ones, hinting that after 3 days of immersion the precipitation of a Ca–P layer had started. A weak bending mode (ν_2) of water ($\sim 1635\text{ cm}^{-1}$) and a broad stretching band of O–H (between 2700 and 3700 cm^{-1} ; the O–H groups are hydrogen bonded [43]) can also be observed in the spectra suggesting that the Ca–P layer already incorporates O–H groups and water molecules from the surrounding fluid. A splitting of the phosphate stretching band, more conspicuous in case of BG-c, could be observed, suggesting a more advanced stage of amorphous calcium phosphates phases’ precipitation [2, 4]. Thus, one can deduce that partial dissolution of BG structure occurred up to 3 days, as demonstrated by the diminishing overall intensity of the spectrum and the lower contribution of

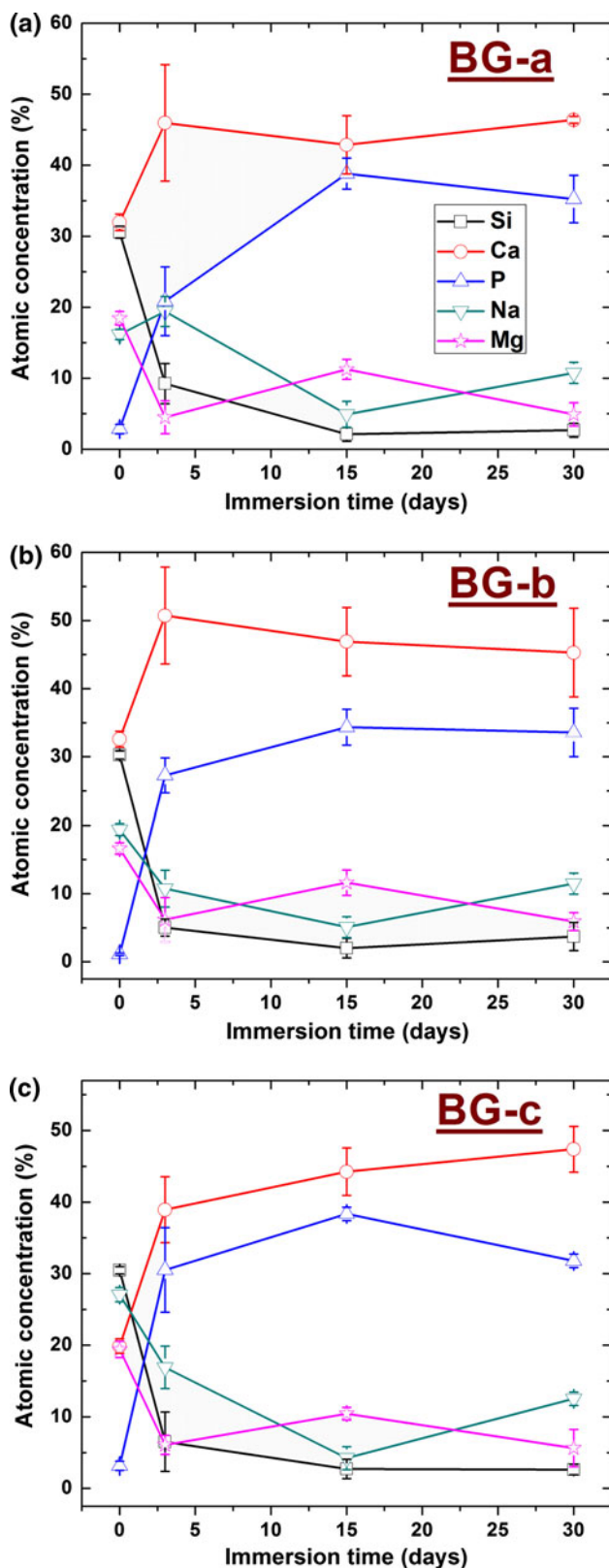


Fig. 6 EDS elemental concentration profiles' evolution with immersion time for Si, Ca, P, Na, and Mg

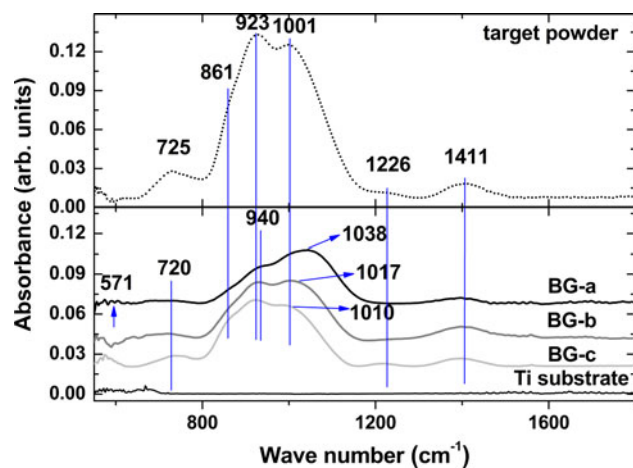


Fig. 7 Comparative FTIR spectra for the powder and studied BG films

Table 5 Assignment of IR vibration bands for the BG films

Vibration band	Sample		
	BG-a	BG-b	BG-c
O–P–O (ν_2) bending mode	483	483	483
Si–O–Si rocking mode	571	571	571
(PO_4) ³⁻ (ν_4) asymmetric bending mode	576	576	576
(PO_4) ³⁻ (ν_4) asymmetric bending mode	612	612	612
Si–O–Si bending mode	720	720	720
Si–O Q ⁰ and Q ¹ units	861	861	861
(CO_3) ²⁻ (ν_2) asymmetric bending mode	876	876	876
P–OH stretching mode of (HPO_4) ²⁻ groups			
Si–O Q ¹ and Q ² units	940	940	940
(PO_4) ³⁻ (ν_1) symmetric stretching mode	960	960	960
Si–O Q ² and Q ³ units	1038	1017	1010
(PO_4) ³⁻ (ν_3) asymmetric stretching mode	1019–1097	1019–1083	1019–1093
Si–O–Si asymmetric stretching	~1100	~1100	~1100
P–OH bending of (HPO_4) ²⁻ groups			
(PO_4) ³⁻ (ν_3') asymmetric stretching mode	1107–1122	1107–1123	1107–1128
B–O stretching of (BO_3) ³⁻ units	1200–1500	1200–1500	1200–1500
(CO_3) ²⁻ (ν_3) asymmetric stretching mode	1413	1413	1413
(CO_3) ²⁻ (ν_3) asymmetric stretching mode	1465	1465	1465
H–O–H (ν_2) bending mode	1635	1635	1635
O–H stretching mode	2700–3700	2700–3700	2700–3700

silicates bands overlapped by the emergence of dominant phosphate bands due to Ca–P precipitation. The leaching of BG ions along with the dissolution-diffusion of silicon atoms from the glass structure resulting in a supersaturation at the film-SBF interface is a prerequisite condition for the starting of precipitation process [4]. One can hypothesize that the peak positioned at $\sim 1125\text{ cm}^{-1}$ could obscure also the presence of Si–O–Si asymmetric stretching vibrations [4, 44], owned to a silica-rich layer formed at the film-solution interface at an early stage. The complex shape of the main vibration maximum, for BG-a and BG-b samples are in agreement with this assumption.

After 15 days (Fig. 8b), all the BG samples displayed similar IR spectra, defined by the phosphate's two intense shoulders positioned around 1028 and 1121 cm^{-1} , respectively. Increases in intensity of water and O–H bands along with the appearance of $(\text{CO}_3)^{2-}$ stretching vibration bands suggest a continuous incorporation of various molecular structures at the liquid–solid interface.

After 30 days of immersion the FTIR absorbance spectra (Fig. 8c) revealed strong vibrations at the following wave numbers: 483, 572, 612, 876, 960, 1019, 1107, 1413, 1465, 1635 and $\sim 3300\text{ cm}^{-1}$, corresponding to crystalline carbonated apatite (CHA). The absorption bands positioned at lower wave numbers could be assigned to bending mode of PÖP Q^3 , Q^2 , Q^1 and Q^0 units ($550\text{--}600\text{ cm}^{-1}$) and, respectively to symmetric stretching bands of PÖP Q^3 , Q^2 and Q^1 units ($650\text{--}800\text{ cm}^{-1}$). The weak band centred at 960 cm^{-1} is assigned to $(\text{PO}_4)^{3-}$ (ν_1) symmetric stretching mode. The sharp bands at 1019 and 1107 cm^{-1} correspond to (ν_3) asymmetric stretching of phosphate groups (Table 5). One should note that the shoulder positioned at the higher wave number could also shadow the presence of a low intensity acid phosphate band. The splitting of the stretching and bending IR absorption bands in two narrow components suggests a crystalline apatitic growth. Additionally one can notice a weak band at 742 cm^{-1} assigned to Si–O–Si bending vibration of the original bioglass films. All apatitic layers obtained were hydroxylated and carbonated as demonstrated by the presence of strong O–H bands (the bending mode centred at $\sim 1635\text{ cm}^{-1}$ and the stretching mode in $2700\text{--}3700\text{ cm}^{-1}$ range) and the sharp C–O bending (ν_2) and stretching (ν_3) lines at (876, 1413 and 1465 cm^{-1}). The vibrational band positioned at 876 cm^{-1} could be the result of the overlapping of the signature band of $(\text{HPO}_4)^{2-}$ with the $(\text{CO}_3)^{2-}$ (ν_2) asymmetric bending mode.

Considering the hydroxyapatite structure, the carbonate group can substitute both the hydroxyl and the phosphate ions, giving rise to the A-type and B-type carbonation, respectively. The positions of the carbonate bands indicate that $(\text{CO}_3)^{2-}$ groups are substituting $(\text{PO}_4)^{3-}$ ions, suggesting the predominance of B-type CHA [45]. The B-type is the preferential substitution in the human bone and is

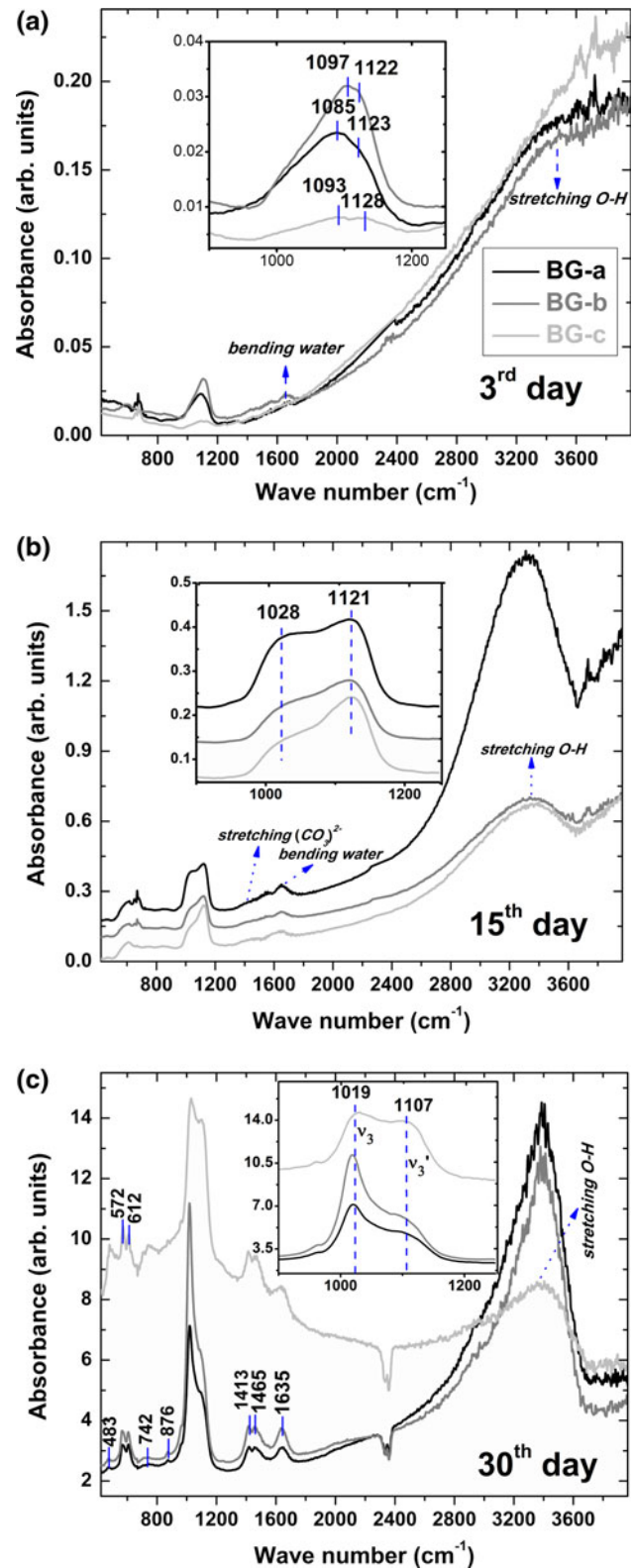


Fig. 8 FTIR spectra evolution with increasing immersion time in SBF

known to have better bioactivity and osteoinductivity [46, 47].

3.6 XRD results

The XRD patterns of the samples immersed in SBF are presented in Fig. 9. The as-deposited films were completely amorphous (results not shown).

The samples show several quite sharp peaks after 3 days of immersion in SBF (Fig. 9a). Since the number of peaks is quite low and they presumably pertain to different phases, the precise phase identification is difficult. Without claiming the uniqueness of the assignments we propose the phase associations marked on Fig. 9. KCl and KCaPO_4 were identified along the immersion period from 3 to 30 days. The presence of calcite was detected in all layers except BG-a. The details in the 2θ range from 25 to 28° presented in Fig. 10 suggest that the route to HA implies several phase transformations. During the first 3 days a sharp maximum arise at $2\theta = 26.6^\circ$ in all BG samples, being especially intense in BG-a. This peak transforms monotonously with increasing soaking time, leading finally to the appearance of the 002 line of HA (Fig. 10). It might be associated with a series of calcium phosphate hydrate phases (i.e. $\text{Ca}(\text{H}_2\text{P}_2\text{O}_7)$ ICDD: 70-6384), or with calcium phosphate hydrate phases with ionic inclusions from the in vitro media (i.e. $\text{CaNa}_2\text{P}_2\text{O}_7(\text{H}_2\text{O})_4$ ICDD: 84-1536). But all these associations are somewhat questionable since several intense lines of whichever of these reference phases do not appear. The apparent absence of some diffraction lines could be due to lattice distortions, since these phases did not present preferential orientations of crystallites as tested by rocking curve measurements (results not shown). To the best of our knowledge, these transformations undergone by BG in SBF were not reported until now, and require more insightful studies to be elucidated.

Diffraction lines characteristic to hydroxyapatite (HA) could be distinguished in all samples after 30 days immersion in SBF (Fig. 9c). The diffraction lines of a reference HA sample (ICDD: 9-432) are represented for comparison at the bottom of the figure. The increased relative intensity of the 002 line is often reported for chemically grown HA layers and it is assigned to the preferred orientation of crystallites [48]. The HA peaks are broad due either to small crystallite sizes or lattice disorders or both. Other sharp diffraction lines arose at $2\theta = 31.4$ and 36.0° , the identification of the first one as NaCl preferentially grown with the cube face parallel to the surface was facilitated by the SEM-EDS analysis, while the best assignment for the second one is $\text{TiH}_{1.7}$ (ICDD: 78-2215). The latter peak is present only in the soaked BG samples, and did not appeared on the Ti control, suggesting that its formation is related to the pH modifications during the dissolution–precipitation processes in SBF.

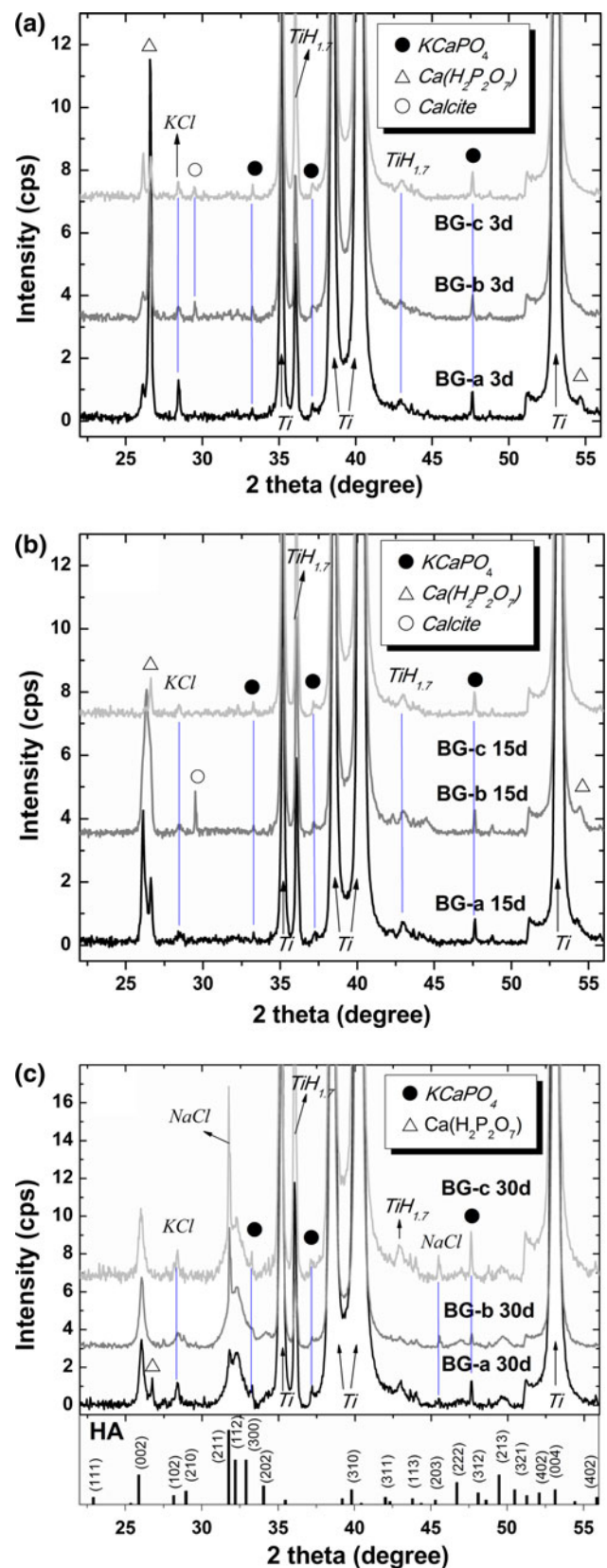


Fig. 9 Comparative representation of the XRD patterns of the as-deposited BG films and after 3, 15 and 30 days immersion in SBF

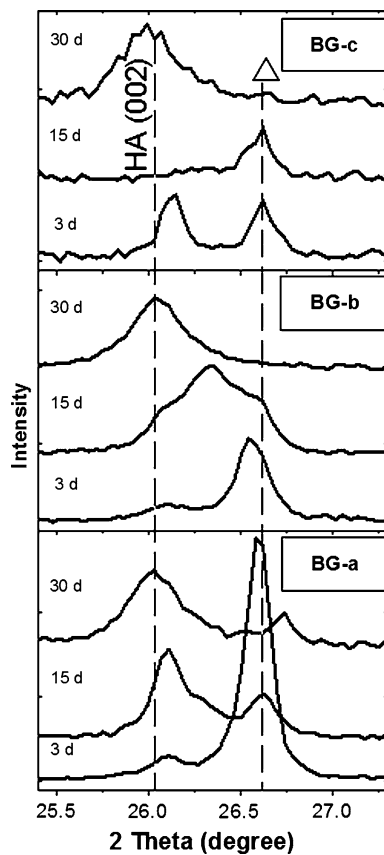


Fig. 10 Details of the XRD diagrams, showing the phase transformations leading to HA

4 Discussion

Thin bioglass films were obtained by magnetron sputtering starting from a novel bioactive powder with low silica content and magnesium oxide, boron oxide, and calcium fluoride additives [21]. By varying the sputtering pressure and working atmosphere we attempted to tailor the films' composition and structure, pursuing optimal mechanical performance and bioactive behaviour. The films were extensively characterized before and after SBF immersion for different times, in order to study and explain their biomineralization behaviour.

The physics of the plasma sputtering process at different working pressures and compositions of the working atmosphere determine also the thicknesses of the as-deposited bioglass films. The films' thicknesses varied between 380 and 510 nm, the thicker for the lowest pressure non-reactive deposition atmosphere. The decrease of the film thickness with the increase of Ar pressure from 0.3 to 0.4 Pa might be assigned to a decreased fraction of sputtered particles reaching the substrate, due to the increased probability of collision with other particles when running from target to substrate. But, despite the masses of the sputtered atoms (M_s) in case of BG material are

comparable to that of the background Ar gas ($M_{Ar}/M_s = 1-1.8$), thus favouring the kinetic energy loss by collision, the thermalization or removal while running towards the substrate is unlikely because of the short target-to-substrate distance (only 30 mm) [49]. Following the studies of Hattum et al. [50] we assume that under these deposition conditions it is highly probable that the main phenomenon leading to decreasing growth rate of BG films is the occurrence of charge transfer reactions in Ar. These processes lead to possible modifications of the energy and extent of the argon ion and neutral bombardment during the deposition in the considered pressure region. The occurrence of resonant charge transfer reactions is known to lower the energy of bombarding ions, determining significant variations of the sputter yield.

The decreased deposition rate observed in the presence of oxygen in the working atmosphere can be attributed to "target poisoning" induced by chemisorption and oxygen ion implantation [51, 52]. During the sputtering process the BG target is bombarded by ions from the plasma, including reactive oxygen ions. This leads to the formation of a compound film not only on the substrate as desired, but also on the sputtering target. This results in a significantly reduced sputter yield, and thereby, a reduced deposition rate [22].

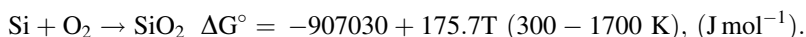
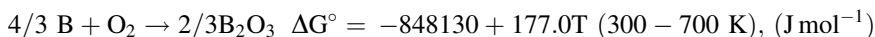
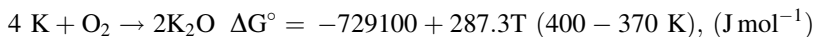
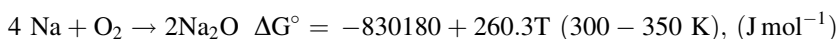
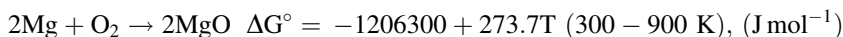
The implant-coating bonding strength plays a definite role on mechanical stability and in vivo performance of the medical device. Excellent results of pull-out adherence (72.6 ± 2.9 MPa) were obtained for the as-deposited BG films when using a 0.3 Pa argon sputtering pressure (BG-a). The bonding strength declined to 45.7 ± 5.0 MPa when increasing the working pressure to 0.4 Pa (BG-b), and to 52.3 ± 3.0 MPa when using a reactive gas mixture with 7% oxygen by keeping the total pressure at a constant value of 0.3 Pa (BG-c).

The high adherence is related to the processes characteristic of magnetron plasma sputtering. At a lower pressure the sputtered atoms collide with the substrate with higher kinetic energy, creating the possibility of forming chemical bonds with atoms from the substrate or being implanted into substrate. Such phenomena could lead to an increased adherence in case of the BG-a films. Using a higher pressure (BG-b) results in a spatial density variation of the background gas and affects the magnetron sputtering discharge as well as the transport of the particles towards the substrate. The energy flux at the substrate is thus affected, which in turn affects the properties of the growing film such as density, grain size, columnar structure, stoichiometry, coverage and adhesion. Moreover, their surface mobility is dramatically reduced, causing possible film inhomogeneities, such as voids or clustering hillocks [53, 54]. In case of films prepared in reactive atmosphere, the presence of tower shaped nano-aggregates on the surface

(BG-c) and of superficial layers enriched in SiO₂, as confirmed by XPS, having high fragility, could be the underlying reasons for the decreased adherence. Usually when dealing with tensile forces, rupture involves only a few molecules in the material causing the whole specimen to fracture in a “domino effect”.

The EDS analysis provides bulk composition, while XPS—which “sees” within around 2 nm in depth—offers information only about the surface composition and chemical state. From EDS, all the BG films have similar amounts of SiO₂ in bulk (Table 4), while XPS showed increased bringing oxygen content in BG-c. Thus, the SiO₂-enrichment of BG-c is only superficial, and might be associated with the particular aggregates observed on the BG-c surface (Fig. 3). One can hypothesize that the occurrence of this phenomenon in reactive atmosphere is related to the increasing poisoning of the target. During the deposition time, the BG target is continuously “poisoned” by the impinging oxygen ions that can be implanted/chemisorbed, turning the target charge more negative, and leading to the binding of alkaline and alkaline-earth elements into the target’s surface, thus making them more difficult to be sputtered. This way the weight of Si in the sputtered BG atomic elements is increased, leading to the formation of the SiO₂ enriched nano-aggregates as deposition progresses.

The reasons for the observed compositional differences between the films obtained from the same target powder under different sputtering conditions, still need to be better understood, requiring a more systematic approach to clarify it in the future. Probably the differences in oxide contents between the glass powder and the deposited coatings have to do with the standard free energy of the oxidation reactions of the different elements involved [55]:



ions at the target’s surface. According to this reasoning, one would expect almost similar concentration changes for Mg since its standard free energy of oxidation is close to that of Ca. However, Table 4 shows that higher concentrations of Mg were determined for all the films in comparison to the starting bioglass powder. This suggests that the atomic weight might also play a role, with heavier elements diffusing more slowly. Na enjoys both of these two characteristics, i.e., it is lighter and its standard free energy of oxidation is lower, being more easily sputtered. The formation of P₄O₁₀, and especially of PO requires higher partial pressure of oxygen. This might explain why a so small amount of P was found in the films. On the other hand, silicon also forms two possible phases, SiO₂ or SiO upon oxidation with the first being favoured at the temperature of the experiments. The formation of these species also requires higher partial pressure of oxygen in comparison to the formation of oxides of Na, Ca, Mg [56, 57]. Monitoring the structure evolution during SBF immersion in case of BG-a, BG-b and BG-c roughly confirmed the Hench model [4]. This theory states that cations from the bioglass surface dissolve in SBF leading to supersaturation of the surrounding fluid with respect to HA elements. The simultaneous dissolution of silicates and hydration results in the formation of silanol groups onto the surface of bioglasses, which are essential nucleation sites for the precipitation and crystallization of apatite. These interactions led to a continuous modification of the BG surface morphology. After 3 days of immersion, nano-sized particles enriched in Ca and P (confirmed by FTIR, XPS and EDS measurements) were uniformly formed onto the surfaces of BG/Ti coatings. Precipitation occurred gradually, granule by granule, until they start merging together forming a dense layer with spherulitic aspect. On the other hand, EDS showed a

Ca is among the most reactive elements towards oxygen, explaining why its concentration decreased in the BG-c films. The reaction between Ca and the impinging oxygen ions might account for target poisoning by binding calcium

decrease of Si, Na and Mg content, during the first stage of immersion. The slowest and the fastest processes were observed for BG-a and BG-c, respectively, with the last one exhibiting the thickest chemically grown HA layer. These

BG coatings exhibit excellent mineralization capability, inducing the formation of extensive apatitic layers onto their surfaces after 30 days of soaking in SBF as revealed by the SEM micrographs (Figs. 4, 5). The presence of CHA in these mineralized layers is clearly demonstrated by XRD. Interestingly, for the all bioactive BG films, a crystalline calcium phosphate (hypothesized to be a calcium phosphate hydrate phase), occurred after 3 days in SBF, the diffraction lines of which almost disappeared after 30 days of immersion, transforming into HA. On the other hand the formation of titanium hydrate phase is known to take place in acidic media. In this condition hydrogen atoms easily diffuse in the interstitial sites of the titanium lattice and dislocations, being absorbed and subsequently react to form TiH_{2-x} . Thus at some point up to 3 days of immersion the pH of the solution was favouring the formation of both TiH_{2-x} and calcium hydrogen phosphate phases.

Leaching alkali and alkali earth ions from the glass into the solution leads in time to the increase of pH and supersaturating of SBF solution that favours HA nucleation. There is a strong possibility that in the SBF solution, in fact a NaCl-rich fluid, could exist also supersaturated regions which could lead at the solid–liquid interface to the formation/precipitation of alkali chlorides. During the rapid exchange of Na and Ca between film and solution, local supersaturating is possible in some regions, leading to the instant precipitation of NaCl. Such phenomena are possible only in vitro tests, where we are dealing with a static fluid, and are highly improbable in vivo, due to the practically infinite quantity of the circulating fluid around the implant.

We hypothesize that such processes occurred during our tests, the composition and the pH of the supersaturated SBF seemed to favour the formation of some salts (NaCl, KCl and $CaCO_3$) which precipitate in sequence during the prolonged immersion (Fig. 9). This presumption is consistent with the increase of Na content starting around day 15 (Fig. 6a–c), and the presence of Cl in these films detected by EDS. Cubic NaCl crystals were detected by SEM/EDS at the surface of Ti substrates (Fig. 4). Therefore, it seems that

the extent of NaCl formation is affected by the supersaturation degree of the solution. Similar observations have been recently reported by Yang et al. [58].

FTIR analysis revealed a general intensity increase of the phosphate and OH groups with immersion time up to 30 days. The shape of vibration bands also changed along the immersion period, which might reflect the evolution of the chemical structures deposited. It is worthy noting that the increasing intensity phosphate bands are obscuring the presence of Si–O–Si asymmetric stretching vibrations [4, 44], of the silica-rich layer formed at the film–solution interface at an early stage. Interestingly, in case of the samples deposited under inert atmosphere (BG-a and BG-b), after 3 days of immersion the breadth of the most prominent peak reduces in comparison to the BG-c samples, showing a possible ordering of the Ca–P precipitated layer, in accordance with the crystallization found by XRD.

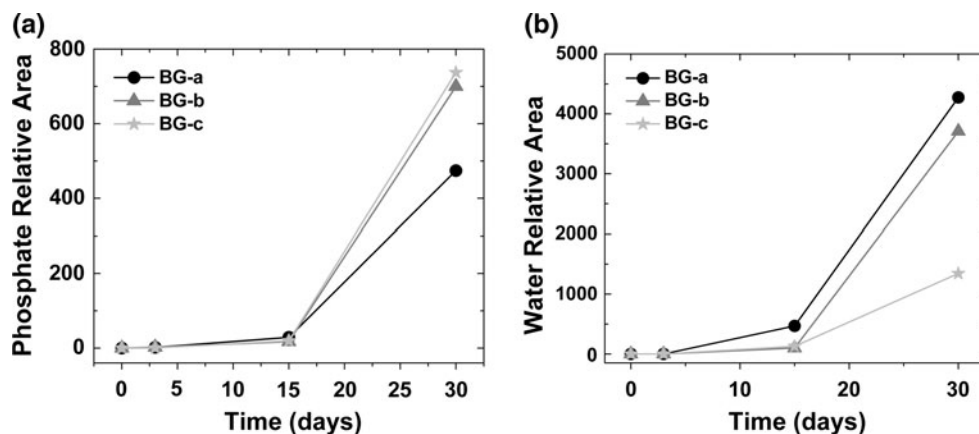
The FTIR analyses suggest that after 15 days of soaking and thereafter structural ordering occurs within the precipitated $CaO-P_2O_5$ layers, resulting in nano-crystalline apatitic layers, the thickness of which increased from BG-a to BG-c.

A detailed analysis of the variations in shape and intensity of the two dominant phosphate bands (ν_3 and ν_3' asymmetric stretching modes) observed along immersion time, could offer interesting insights on the in vitro behaviour of sputtered BG films. The intensity variations are similar during the growth process:

- at 3 days, ν_3 intensity $\sim \nu_3'$ intensity
- at 15 days, ν_3 intensity $< \nu_3'$ intensity
- at 30 days ν_3 intensity $> \nu_3'$ intensity.

Figure 11a displays the dependence of $(PO_4)^{3-}$ integral area of asymmetric stretching band up to 30 days. This area can be roughly approximated with the mass of the chemical grown films, so could be more or less an indicator of the films bioactivity degree. The degree of hydroxylation of the films (integral area of O–H stretching band) is displayed in Fig. 11b.

Fig. 11 The relative intensities of the P–O (a) and O–H (b) IR stretching bands versus immersion time in SBF



From the evolution of phosphate bands, it can be noticed once more the slower growing rate of Ca–P layer for BG-a, while for BG-b and BG-c there is a steep and continuous increase of P–O intensity of stretching band which starts at a moment around 15 days. This could be due to the nucleation process which consists in a continuous supersaturation of interface by film dissolution and which precede the effective process of chemical growth.

One can see that for all BG samples the P–O stretching intensity starts to slowly increase after 3 days, the precipitation rate being accelerated after 15 days of immersion (Fig. 11a). Besides, after 3 days of immersion the ratio of the ν_3/ν_3' intensities is roughly constant (Fig. 8a). This suggests that some kind of dissolution–reprecipitation occurs at the film-SBF interface until the end of growth process as illustrated by the clear modification of ν_3/ν_3' intensities ratio from 15 to 30 days. Accordingly, the structure of deposited Ca–P layers is continuously changing along the growth process. Moreover, one could expect a longer Ca–P growth saturation time interval for BG-b and BG-c samples, then for BG-a.

The water incorporation kinetics (Fig. 11b) suggests that the apatitic layer grown onto BG-c after 30 days of immersion is less hydroxylated in comparison to those precipitated onto the BG-a and BG-b samples deposited under inert atmosphere. According to Pasteris et al. [59], a reduced hydroxylation might enhance the formation of mineral–collagen bond and increase the solubility in biological media. On the other hand, apatitic structures with higher OH content might be welcome for dental implantology applications due to their higher buffering capacity, and thus augment the resistance against the local acidic media.

In order to explain the higher biomineralization rates of BG-b and BG-c films one can hypothesize that the chemical processes involved in the bioactivity mechanism are accelerated, because of the increased sodium content of these films (Table 4), speeding up the ionic exchange and the chemical growth of HA. Hench's theory states that the first stage of SBF immersion of a bioglass involves the rapid exchange of Na^+ ions from the glass for H^+ and H_3O^+ ions from the solution, which shall initialize the formation of silica-rich layer known to favour the nucleation of Ca–P type layers. Therefore, we can suppose that a higher number of sodium ions released into SBF solution will change the chemical equilibrium of the precipitation reaction, thereby catalyzing the CHA chemical growth mechanism.

5 Conclusions

Thin bioglass films (380–510 nm) were deposited by radio-frequency magnetron sputtering onto medical grade

titanium substrates starting from a novel bioactive powder with low silica content and MgO , B_2O_3 , and CaF_2 additives. Extensive studies upon the influence of working conditions (pressure, atmosphere) on morphology, structure, composition, bonding strength and in vitro bioactive properties of sputtered BG films were performed.

Excellent results of pull-out adherence were obtained when using a 0.3 Pa argon sputtering pressure (BG-a). The bonding strength declined when increasing the working pressure to 0.4 Pa (BG-b) or when using a reactive gas mixture, keeping the total pressure at constant value of 0.3 Pa (BG-c).

The simulated body fluid tests clearly demonstrated strong bioactive features for the all BG films. The biomineralization rate increased from BG-a to BG-b, and yet more for BG-c. The morpho-structural and compositional monitoring of BG films in vitro behaviour confirmed roughly the Hench bioactivity model. An interesting result was the development of a well-crystallized phase (presumably a calcium phosphate hydrate phase) on the BG layer after 3 days of immersion in SBF for all the films.

The study indicated that the composition and structure along with essential properties of BG films (adhesion, bioactivity) can be tailored simply by altering the magnetron deposition conditions. By varying the composition and therefore the level of disruption in the glass network, the production of bioglass coatings with desirable physical and biological properties should become feasible.

Acknowledgments Thanks are due to CICECO for the support and to the Portuguese Foundation for Science and Technology for the fellowship grants of S. Pina (FRH/BPD/64119/2009) and A.F. Lemos (SFRH/BPD/27046/2006), and to Romanian Ministry of Education and Research for the financial support of Core Program—Contract PN09-45 and ID 76 scientific projects. Authors are grateful to Cristian-Mihail Teodorescu for the professional assistance with XPS measurements.

References

1. Hench LL, Splinter RJ, Allen WC, Greenlee TK. Bonding mechanism at the interface of ceramic prosthetic materials. *J Biomed Mater Res Symp.* 1971;2:117–41.
2. Hench LL, Wilson J. Introduction to bioceramics. In: Hench LL, Wilson J, editors. Singapore: World Scientific Publishing Company; 1993.
3. Ratner BD, Hoffman AS, Schoen FJ, Lemons JE. Biomaterials science. In: Ratner BD, Hoffman AS, Schoen FJ, Lemons JE, editors. An introduction to materials in medicine. New York: Academic Press; 2004.
4. Hench LL. Bioceramics: from concept to clinic. *J Am Ceram Soc.* 1991;74:1487–91.
5. Wilson J, Yli-Urpo A, Risto-Pekka H. Bioactive glasses: clinical applications. In: Hench LL, Wilson J, editors. An introduction to bioceramics. Singapore: World Scientific Publishing Company; 1993. p. 63–74.

6. Kasuga T, Sawada M, Nogami M, Abe Y. Bioactive ceramics prepared by sintering and crystallization of calcium phosphate invert glasses. *Biomaterials*. 1999;20:1415–20.
7. Kokubo T. Surface chemistry of bioactive glass-ceramics. *J Non Cryst Solids*. 1990;120:138–51.
8. Cao W, Hench LL. Bioactive materials. *Ceramics Int*. 1996; 22:493–507.
9. Kokubo T. A/W glass-ceramic: Processing and properties. In: Hench LL, Wilson J, editors. *Introduction to bioceramics*. Singapore: World Scientific Publishing Company; 1993. p. 75–88.
10. Hench LL. Bioactive ceramics: theory and clinical applications. In: Andersson OH, Yli-Urpo A, editors. *Bioceramics 7*. Oxford: Butterworth-Heinemann Ltd.; 1994. p. 3–14.
11. Hench LL, West JK. Biological applications of bioactive glasses. *Life Chem Rep*. 1996;13:187–241.
12. Saiz E, Goldman M, Gomez-Vega JM, Tomsia AP, Marshall GW, Marshall SJ. In vitro behavior of silicate glass coatings on Ti6Al4V. *Biomaterials*. 2002;23:3749–56.
13. Izquierdo-Barba I, Conde F, Olmo N, Lizarbe MA, Garcia MA, Vallet-Regi M. Vitreous SiO₂-CaO coatings on Ti6Al4V alloys: reactivity in simulated body fluid versus osteoblast cell culture. *Acta Biomater*. 2006;2:445–55.
14. Lopez-Esteban S, Saiz E, Fujino S, Oku T, Suganuma K, Tomsia AP. Bioactive glass coatings for orthopedic metallic implants. *J Eur Cer Soc*. 2003;23:2921–30.
15. Popescu AC, Sima F, Duta L, Popescu C, Mihailescu IN, Capitanu D, Mustata R, Sima LE, Petrescu SM, Janackovic D. Biocompatible and bioactive nanostructured glass coatings synthesized by pulsed laser deposition: In vitro biological tests. *Appl Surf Sci*. 2009;255:5486–90.
16. Mardare CC, Mardare AI, Fernandes JRF, Joannia E, Pina SCA, Fernandes MHV, Correia RB. Deposition of bioactive glass-ceramic thin-films by RF magnetron sputtering. *J Eur Ceram Soc*. 2003;23:1027–30.
17. Goller G. The effect of bond coat on mechanical properties of plasma sprayed bioglass-titanium coatings. *Ceram Int*. 2004;30: 351–5.
18. Wolke JGC, van den Beucken JJJP, Jansen JA. Growth behaviour of rat bone marrow cells on RF magnetron sputtered bioglass and calcium phosphate coatings. *Key Eng Mater*. 2008;361(363): 253–6.
19. Saino E, Maliardi V, Quartarone E, Fassina L, Benedetti L, De Angelis MG, Mustarelli P, Facchini A, Visai L. In vitro enhancement of SAOS-2 cell calcified matrix deposition onto radio frequency magnetron sputtered bioglass-coated titanium scaffolds. *Tissue Eng Part A*. 2010;16:995–1008.
20. Wasa K, Kitabatake M, Adachi H. Thin film materials technology: sputtering of compound materials. New York: Noyes Publications; 2003.
21. Agathopoulos S, Tulyaganov DU, Ventura JMG, Kannan S, Karakassides MA, Ferreira JMF. Formation of hydroxyapatite onto glasses of the CaO-MgO-SiO₂ system with B₂O₃, Na₂O, CaF₂ and P₂O₅ additives. *Biomaterials*. 2006;27:1832–40.
22. Stan GE, Pina S, Tulyaganov DU, Ferreira JMF, Pasuk I, Morosanu CO. Biomineralization capability of adherent bio-glass films prepared by magnetron sputtering. *J Mater Sci Mater Med*. 2010;21:1047–55.
23. Swanepoel RJ. Determination of the thickness and optical constants of amorphous silicon. *J Phys E*. 1983;16:1214–22.
24. Stan GE, Morosanu CO, Marcov DA, Pasuk I, Miculescu F, Reumont G. Effect of annealing upon the structure and adhesion properties of sputtered bio-glass/titanium coatings. *Appl Surf Sci*. 2009;255:9132–8.
25. Mardare D, Luca D, Teodorescu CM, Macovei D. On the hydrophilicity of nitrogen-doped TiO₂ thin films. *Surf Sci*. 2007; 601:4515–20.
26. Teodorescu CM, Esteva JM, Kainatak RC, El Afif A. An approximation of the Voigt I profile for the fitting of experimental X-ray absorption data. *Nucl Instrum Methods Phys Res Sect A*. 1994;345:141–7.
27. Kokubo T, Kushitani H, Ohtsuki C, Sakka S, Yamamuro T. Effects of ions dissolved from bioactive glass-ceramic on the surface apatite formation. *J Mater Sci Mater Med*. 1993;4:1–4.
28. Kokubo T, Takadama H. How useful is SBF in predicting in vivo bone bioactivity? *Biomaterials*. 2006;27:2907–15.
29. Peddi L, Brow RK, Brown RF. Bioactive borate glass coatings for titanium alloys. *J Mater Sci Mater Med*. 2008;19:3145–52.
30. Serra J, González P, Liste S, Chiussi S, León B, Pérez-Amor M, Ylänen HO, Hupa M. Influence of the non-bridging oxygen groups on the bioactivity of silicate glasses. *J Mater Sci Mater Med*. 2002;13:1221–5.
31. Liste S, Serra J, González P, Borrajo JP, Chiussi S, León B, Pérez-Amor M. The role of the reactive atmosphere in pulsed laser deposition of bioactive glass films. *Thin Solid Films*. 2004; 453–454:224–8.
32. Goldman DS. Evaluation of the ratios of bridging to nonbridging oxygens in simple silicate glasses by electron spectroscopy for chemical analysis. *Phys Chem Glasses*. 1986;27:128–33.
33. Bunker BC, Tallant DR, Kirkpatrick RJ, Turner GL. Multinuclear magnetic resonance and Raman investigation of sodium borosilicate glass structures. *Phys Chem Glasses*. 1990;31:30–41.
34. Brow RK, Kirkpatrick RJ, Turner GL. The short range structure of sodium phosphate glasses I. MAS NMR studies. *J Non Cryst Solids*. 1990;116:39–45.
35. Brinen JL, White MG. Postsynthesis modification of alum inophosphates by reaction with silicon tetrachloride. *J Catal*. 1990;124:133–47.
36. Nanba T, Nishimura M, Miura Y. A theoretical interpretation of the chemical shift of ²⁹Si NMR peaks in alkali borosilicate glasses. *Geochim Cosmochim Acta*. 2004;68:5103–11.
37. Luca D, Teodorescu CM, Apetrei R, Macovei D, Mardare D. Preparation and characterization of increased-efficiency photocatalytic TiO_{2-2x}N_x thin films. *Thin Solid Films*. 2007;515: 8605–10.
38. Tuttle PV, Rundell AE, Webster TJ. Influence of biologically inspired nanometer surface roughness on antigen-antibody interactions for immunoassay-biosensor applications. *Int J Nanomed*. 2006;1:497–505.
39. Price RL, Gutwein LG, Kaledin L, Tepper F, Webster TJ. Osteoblast function on nanophase alumina materials: influence of chemistry, phase, and topography. *J Biomed Mater Res Part A*. 2003;67:1284–93.
40. Webster TJ, Siegel RW, Bizios R. Osteoblast adhesion on nanophase ceramics. *Biomaterials*. 1999;20:1221–7.
41. Lopez-Esteban S, Gutierrez-Gonzalez CF, Gremillard L, Saiz E, Tomsia AP. Interfaces in graded coatings on titanium-based implants. *J Biomed Mater Res Part A*. 2009;88:1010–21.
42. Balamurugan A, Balossier G, Kannan S, Michel J, Rebelo AHS, Ferreira JMF. Development and in vitro characterization of sol-gel derived CaO-P₂O₅-SiO₂-ZnO bioglass. *Acta Biomater*. 2007;3:255–62.
43. Ruban Kumar A, Kalainathan S. Growth and characterization of nano-crystalline hydroxyapatite at physiological conditions. *Cryst Res Technol*. 2008;43:640–4.
44. Socrates G. *Infrared and Raman characteristic group frequencies—tables and charts*. Chichester: John Wiley & Sons Ltd; 2007.
45. Markovic M, Fowler BO, Tung MS. Preparation and comprehensive characterization of a calcium hydroxyapatite reference material. *J Res Natl Inst Stand Technol*. 2004;109:553–68.
46. Landi E, Celotti G, Logroscino G, Tampieri A. Carbonated hydroxyapatite as bone substitute. *J Eur Ceram Soc*. 2003;23: 2931–7.

47. Rey C, Collins B, Goehl T, Dickson IR, Glimcher MJ. The carbonate environment in bone mineral: a resolution enhanced fourier transform spectroscopy study. *Calcif Tissue Int.* 1989;45: 157–64.
48. Hong Z, Luan L, Paik SB, Deng B, Ellis DE, Ketterson JB, Mello A, Eon JG, Terra J, Rossi A. Crystalline hydroxyapatite thin films produced at room temperature—an opposing radio frequency magnetron sputtering approach. *Thin Solid Films.* 2007;515: 6773–80.
49. Palmero A, Rudolph H, Habraken FHPM. One-dimensional analysis of the rate of plasma-assisted sputter deposition. *J Appl Phys.* 2007;101:083307–083307-6.
50. van Hattum ED, Palmero A, Arnoldbik WM, Rudolph H, Habraken FHPM. On the ion and neutral atom bombardment of the growth surface in magnetron plasma sputter deposition. *Appl Phys Lett.* 2007;91:171501–171501-3.
51. Güttler D, Abendroth B, Grotzschel R, Moller W, Depla D. Mechanisms of target poisoning during magnetron sputtering as investigated by real-time in situ analysis and collisional computer simulation. *Appl Phys Lett.* 2004;85(25):6134–6.
52. Berg S, Nyberg T. Fundamental understanding and modeling of reactive sputtering processes. *Thin Solid Films.* 2005;476(2): 215–30.
53. Ekpe SD, Dew SK. 3D numerical simulation of gas heating effects in a magnetron sputter deposition system. *J Phys D.* 2006; 39:1413–21.
54. Stan GE, Marcov DA, Pasuk I, Miculescu F, Pina S, Tulyaganov DU, Ferreira JMF. Bioactive glass thin films deposited by magnetron sputtering technique: the role of working pressure. *Appl Surf Sci.* 2010;256:7102–10.
55. Alcock CB. *Thermochemical processes—principles and models.* Oxford: Butterworth-Heinemann; 2001. p. 384.
56. http://www.doitpoms.ac.uk/tlplib/ellingham_diagrams/ellingham.php.
57. http://www.doitpoms.ac.uk/tlplib/ellingham_diagrams/interactive.php.
58. Yang L, Hedhammar M, Blom T, Leifer K, Johansson J, Habibovic P, van Blitterswijk CA. Biomimetic calcium phosphate coatings on recombinant spider silk fibres. *Biomed Mater.* 2010;5:045002–12.
59. Pasteris JD, Wopenk B, Freeman JJ, Rogers K, Valsami-Jones E, van der Houwen JAM, Silva MJ. Lack of OH in nanocrystalline apatite as a function of degree of atomic order: implications for bone and biomaterials. *Biomaterials.* 2004;25:229–38.